



## Realization of all-in-one hydrogen-evolving photocatalysts via selective atomic substitution

Bocheng Qiu <sup>a,\*,\*\*</sup>, Pan Huang <sup>c</sup>, Cheng Lian <sup>c, \*\*</sup>, Yingxin Ma <sup>a</sup>, Mingyang Xing <sup>b</sup>, Honglai Liu <sup>c</sup>, Jinlong Zhang <sup>b,d,\*</sup>

<sup>a</sup> Jiangsu Key Laboratory of Pesticide Sciences, Department of Chemistry, College of Sciences, Nanjing Agricultural University, Nanjing, 210095, PR China

<sup>b</sup> Shanghai Engineering Research Center for Multi-Media Environmental Catalysis and Resource Utilization, Key Laboratory for Advanced Materials and Joint International Research Laboratory of Precision Chemistry and Molecular Engineering, Feringa Nobel Prize Scientist Joint Research Center, School of Chemistry and Molecular Engineering, East China University of Science & Technology, Shanghai, 200237, PR China

<sup>c</sup> State Key Laboratory of Chemical Engineering, Shanghai Engineering Research Center of Hierarchical Nanomaterials, School of Chemistry and Molecular Engineering, East China University of Science and Technology, Shanghai, 200237, PR China

<sup>d</sup> School of Chemistry & Chemical Engineering, Yancheng Institute of Technology, Yancheng, 224051, PR China



### ARTICLE INFO

#### Keywords:

Selective substitution  
Charge separation  
Hydrogen adsorption and desorption  
Photocatalytic hydrogen evolution

### ABSTRACT

Major challenges of realization of all-in-one hydrogen-evolving photocatalysts are the relatively poor charge separation efficiency and unfavorable hydrogen desorption properties owing to the strong correlation between the catalytic site and adsorbed H. Herein, an example of Ni doped few-layer ZnIn<sub>2</sub>S<sub>4</sub> nanosheets (Ni-ZnIn<sub>2</sub>S<sub>4</sub>) is carried out to deeply understand the role of Ni dopant in tailoring the charge separation efficiency and weakening the bond energy between electronegative S sites and adsorbed H (S-H<sub>ads</sub>). Our theoretical calculations demonstrate that Ni ions preferentially incorporates into tetrahedral Zn sites rather than tetrahedral/octahedral In sites, which endows Ni-ZnIn<sub>2</sub>S<sub>4</sub> with improved electronic conductivity and more delocalized charge carriers involved in hydrogen evolution reaction (HER). More importantly, Ni dopants can be capable of exquisitely altering the electronic structure of S sites, leading to a balanced hydrogen adsorption and desorption ability. Consequently, the as-prepared few-layer Ni-ZnIn<sub>2</sub>S<sub>4</sub> nanosheets enable long-lived photo-excited electrons and enhanced photocatalytic HER performance.

### 1. Introduction

Solar-light driven water splitting into hydrogen on semiconductor provides a promising route to tackle the energy crisis and environmental pollution issues [1–5]. Nevertheless, most of discovered semiconductor photocatalysts inevitably suffer from low hydrogen evolution reaction (HER) performance, which is far from the industrial application. Specifically, the ineffective charge separation and migration, and poor hydrogen adsorption and desorption capability, are the two main limitations that severely impeding their photocatalytic HER activity [6–10]. Recently, semiconductor materials based on ternary metal sulfides have gained widespread attention due to their earth abundance, strong visible light absorption ability as well as accessible synthesis process [11–13].

Taking zinc indium sulfide (ZnIn<sub>2</sub>S<sub>4</sub>) as an example [14–17], ZnIn<sub>2</sub>S<sub>4</sub> with stacked structure of S-Zn-S-In-S-In-S layers enables a well-suited band structure and a favorable hydrogen absorption ability on S sites, hence favoring it as a promising HER photocatalyst. Particularly, the valence band (VB) of ZnIn<sub>2</sub>S<sub>4</sub> principally consists of S 3p orbitals, which display much more negative potentials relative to that of O 2p orbitals in metal oxides, thereby giving rise to narrow band gap to harness solar energy [18–20]. On the other hand, the bottom of conduction band (CB) for ZnIn<sub>2</sub>S<sub>4</sub> is mainly comprised of empty metal d orbitals, which endows the photo-induced electron with high reduction potential and thus benefits the HER performance [21–25]. Furthermore, the H atoms are easily adsorbed (H<sub>ads</sub>) on the surface of ZnIn<sub>2</sub>S<sub>4</sub> via the formation of S—H<sub>ads</sub> bond, which lowers down H adsorption energy [26,27]. Despite

\* Corresponding author at: Shanghai Engineering Research Center for Multi-Media Environmental Catalysis and Resource Utilization, Key Laboratory for Advanced Materials and Joint International Research Laboratory of Precision Chemistry and Molecular Engineering, Feringa Nobel Prize Scientist Joint Research Center, School of Chemistry and Molecular Engineering, East China University of Science & Technology, Shanghai, 200237, PR China.

\*\* Corresponding author.

E-mail addresses: [bochengqiu@njau.edu.cn](mailto:bochengqiu@njau.edu.cn) (B. Qiu), [liancheng@ecust.edu.cn](mailto:liancheng@ecust.edu.cn) (C. Lian), [jlzhang@ecust.edu.cn](mailto:jlzhang@ecust.edu.cn) (J. Zhang).

these strengths, the photocatalytic HER performance of  $\text{ZnIn}_2\text{S}_4$  remains still low owing to the following two issues: 1)  $\text{ZnIn}_2\text{S}_4$  suffers from a serious recombination of photo-generated electron-hole pairs; 2) the  $\text{H}_{\text{ads}}$  is securely immobilized on S sites in the form of  $\text{S}-\text{H}_{\text{ads}}$  bond, which increases the difficulty of the hydrogen desorption from S sites. Consequently, developing a feasible strategy to achieve the integration of superior charge separation and balanced H adsorption/desorption on a single semiconductor photocatalyst is extremely desirable.

Exotic atoms doping has been regarded as an effective approach to extend the light absorption range, increase the surface catalytic sites, and modulate the H adsorption and desorption properties [28–31]. Up to now, despite the fact that the positive effect of element doping on photocatalytic activity is validated by the remarkably previous literature, there exist some studies with totally reverse description for the role of heteroatom dopant. As an example, the exotic atoms within the bulk structure of photocatalysts may serve as a recombination site of photo-induced charge carriers, which is detrimental to the improvement of the photocatalytic performance [32–34]. Moreover, as for bulk dopant, it seems to be difficult to have an impact on the H adsorption and desorption behaviors on surface S sites [35]. To this end,  $\text{ZnIn}_2\text{S}_4$  nanosheets with ultrathin structure provide an accessible surface to achieve surface element doping, which helps to offering an in-depth understanding of the underlying correlations between the dopant and photocatalytic performance at atomic scale. Moreover, the ultrathin 2D  $\text{ZnIn}_2\text{S}_4$  nanosheets enable a shortened bulk diffusion distance to reduce the bulk recombination rate of charge-carriers, and abundant catalytic sites to facilitate the HER kinetics [36–39].

Herein, we first employed density function theory (DFT) simulations to predict a potential HER activity in Ni doped few-layer  $\text{ZnIn}_2\text{S}_4$  nanosheets (denoted as  $\text{Ni-ZnIn}_2\text{S}_4$ ) via calculating their electronic structure. Experimentally, we employ a solvothermal method to incorporate Ni cations into the lattices of  $\text{ZnIn}_2\text{S}_4$  with preferred tetrahedral Zn occupation, which agrees with the theoretical prediction well. Specifically, combined with theoretical calculations and experimental analysis, Ni doping into tetrahedral Zn sites can induce an increased electronic conductivity and electron delocalization of Ni sites on  $\text{ZnIn}_2\text{S}_4$  as well as a facilitated H desorption ability, which collectively promotes HER performance. As expected, the as-prepared  $\text{Ni-ZnIn}_2\text{S}_4$  nanosheets with the optimal Ni doping level possess an enhanced photocatalytic HER activity of  $5.43 \text{ mmol g}^{-1} \text{ h}^{-1}$ , roughly 7 times higher than bare  $\text{ZnIn}_2\text{S}_4$  nanosheets. This work offers new insights to engineer electronic structure in metal sulfides for efficient photocatalysis.

## 2. Experimental section

### 2.1. Preparation of $\text{ZnIn}_2\text{S}_4$ nanosheets

Typically, 0.4 mmol  $\text{Zn}(\text{CH}_3\text{COO})_2$  and 0.8 mmol  $\text{InCl}_3$  were added into the mixed solvent containing 15 mL  $\text{H}_2\text{O}$  and 15 mL ethanol. After stirring for 30 min, 3.2 mmol thiouacetamide was dissolved into the above solution. After another 30 min's stirring, the solution was transferred into a 50 mL Teflon-lined stainless steel autoclave and kept at 180 °C for 24 h. After cooling down, the  $\text{ZnIn}_2\text{S}_4$  product was collected by centrifugation and subsequently washed by  $\text{H}_2\text{O}$  and ethanol for three times, and finally vacuum-dried at 40 °C.

### 2.2. Preparation of $\text{Ni-ZnIn}_2\text{S}_4$ nanosheets

Typically, 0.4 mmol  $\text{Zn}(\text{CH}_3\text{COO})_2$ , 0.8 mmol  $\text{InCl}_3$ , and 0.03 mmol  $\text{Ni}(\text{CH}_3\text{COO})_2$  were dissolved into the mixed solvent containing 15 mL  $\text{H}_2\text{O}$  and 15 mL ethanol. After stirring for 30 min, 3.2 mmol thiouacetamide was added into the above solution. After another 30 min's stirring, the solution was transferred into a 50 mL Teflon-lined stainless steel autoclave and kept at 180 °C for 24 h. After cooling down, the  $\text{Ni-ZnIn}_2\text{S}_4$  product was collected by centrifugation and washed by  $\text{H}_2\text{O}$  and ethanol for three times, and vacuum-dried at 40 °C. The Ni doping

concentration is 1.0 wt % detected by inductively coupled plasma mass spectrometry (ICP-MS). By changing the addition amount of  $\text{Ni}(\text{CH}_3\text{COO})_2$  (0.01 mmol, 0.02 mmol, 0.04 mmol, and 0.05 mmol), the samples with different Ni doping levels (0.4 wt %, 0.8 wt %, 1.4 wt %, and 1.8 wt %) can be obtained.

## 2.3. Characterizations

The morphologies and composition of all the samples were recorded by using a JEM-2100F high resolution transmission electron microscopy at an accelerated voltage of 300 kV. An energy-dispersive X-ray detector (Oxford X-MAX 80 T) attached on JEM-2100F was employed to analyze element composition. X-ray diffraction (XRD) patterns with the range from 5 to 80° (2θ) were collected by using a RigakuD/MAX IIIA diffract meter operated at 40 kV and 100 mA with  $\text{Cu K}\alpha$  irradiation ( $\lambda = 1.5418 \text{ \AA}$ ). XPS data were collected by using a Perkin-Elmer PHI 5000C ESCA system with  $\text{Al K}\alpha$  irradiation operated at 250 W. The concentrations of Ni dopants were determined by ICP-MS (Agilent 7700x). The nitrogen adsorption and desorption curves were recorded on a surface area analyzer (ASAP2020) at 77 K after degassing the samples at 120 °C for 4 h. The steady-state PL emission and time-resolved PL spectra were conducted at room temperature by using fluorescence spectrophotometer (Edinburgh FLS980). Photocurrent responses were performed under chopped illumination and recorded on the electrochemical workstation (CHI660E) combined with a standard three electrode cell consisting of a working electrode, a counter electrode (graphite rod), and a reference electrode (saturated calomel). The initial bias voltage in the photocurrent tests was determined to be 0 V (E vs.  $E_{\text{calomel}}$ ). Electrochemical impedance measurements were carried out on the electrochemical workstation (CHI660E) in the frequency range from 0.01 to 100k Hz. The working electrode was prepared via deposition of powder samples on a clean fluoride-tin oxide (FTO), and  $\text{Na}_2\text{SO}_4$  solution (0.5 M) was used as the electrolyte. Linear sweep voltammetry (LSV) curves for  $\text{ZnIn}_2\text{S}_4$  and  $\text{Ni-ZnIn}_2\text{S}_4$  were collected at a constant scan rate (5 mV s<sup>-1</sup>) on the electrochemical workstation (CHI660E).

## 2.4. Theoretical calculations

The first-principles density function theory (DFT) calculations were implemented in the Vienna Ab initio Simulation Package (VASP), which used the projector augmented plane-wave (PAW) method [40–42] to spans reciprocal space with a plane-wave basis. All calculations were performed within the generalized-gradient approximation (GGA) with the exchange-correlation functional of Perdew-Burke-Ernzerhof (PBE). For the plane-wave basis set, the energy cutoff was set to  $E_{\text{cut}} = 500 \text{ eV}$ , and the positions of the atoms were allowed to relax until the energy and force were less than  $10^{-4} \text{ eV}$  and  $0.01 \text{ eV}/\text{\AA}$ , respectively. A 3\*3\*2 supercell with 126 atoms was used for the calculation of the optimal structure. For the Ni-doped  $\text{ZnIn}_2\text{S}_4$  model, either Zn or In atoms were replaced by one or two Ni atoms in  $\text{ZnIn}_2\text{S}_4$ . The adsorption free energy of  $\text{H}^*$  ( $\Delta G_{\text{H}^*}$ ), for describing the activity of hydrogen evolution reaction (HER) in  $\text{ZnIn}_2\text{S}_4$  or  $\text{Ni-ZnIn}_2\text{S}_4$ , can be obtained by correcting the differential binding energy of  $\text{H}^*$  ( $\Delta E_{\text{H}^*}$ ).  $\Delta E_{\text{H}^*}$  describes the stability of H atoms, defined by  $\Delta E_{\text{H}} = E(\text{ZnIn}_2\text{S}_4 + \text{H}) - E(\text{ZnIn}_2\text{S}_4) - 1/2E(\text{H}_2)$ , where  $E(\text{ZnIn}_2\text{S}_4 + \text{H})$  represents the total binding energy of the  $\text{ZnIn}_2\text{S}_4$  or  $\text{Ni-ZnIn}_2\text{S}_4$  with one adsorbed H atom,  $E(\text{ZnIn}_2\text{S}_4)$  is the total energy of  $\text{ZnIn}_2\text{S}_4$  or  $\text{Ni-ZnIn}_2\text{S}_4$  without H atoms, and  $E(\text{H}_2)$  is the energy of a gas phase hydrogen molecule. Significantly, for metal catalysts,  $\Delta G_{\text{H}^*}$  is modified by  $\Delta G_{\text{H}^*} = \Delta E_{\text{H}} + 0.24 \text{ eV}$ .

## 2.5. Photocatalytic hydrogen evolution reaction

Photocatalytic hydrogen evolution reactions were carried out on an online sealed Pyrex photocatalysis system (Labsolar-6A, Beijing Perfectlight) at constant temperature (5 °C) under a simulated sunlight illumination (AM 1.5 G). 50 mg of catalyst was added into 100 mL of

aqueous solution containing 10 mL triethanolamine (TEOA) as an electron donor and sonicated for 30 min. Afterward, the suspension was degassed for 30 min. Generated gas ( $H_2$ ) was analyzed by a Fuli GC9790 gas chromatograph (molecular sieve column with Ar as the carrier gas). As for the cycle photocatalytic tests, when one cycle test of 4 h was finished, 10 mL TEOA was re-added into the mixture before initiating the next cycle. The measurement of the quantum efficiency (QE) for HER was conducted under the illumination of a 300 W Xe lamp with various bandpass filters. The number of incident photons ( $N$ ) was measured by a fibre spectrometer and further calculated according to Eq. (1). The QE value was calculated in terms of Eq. (2).

$$N = \frac{E\lambda}{hc} \quad (1)$$

$$QE = \frac{\text{Number of the evolved } H_2 \text{ molecules} * 2}{N} \quad (2)$$

### 3. Results and discussion

#### 3.1. Theoretical investigations of Ni doping effects

Here, we first use well-defined  $ZnIn_2S_4$  model to illustrate the coordination environment of metal atoms in  $ZnIn_2S_4$ . As shown in Fig. 1a,  $ZnIn_2S_4$  has a layered hexagonal structure, in which Zn atoms are paired with the S tetrahedron and In atoms are coordinated with S tetrahedron

or S octahedron. We further employed theoretical calculations to demonstrate preference position of Ni dopant in  $ZnIn_2S_4$  atomic layers. As indicated in Fig. 1b, the calculated total energy of one Ni atom doping into tetrahedral Zn site in  $ZnIn_2S_4$  is  $-485.37$  eV, which is lower than that doping into tetrahedral In site ( $-483.83$  eV) (Fig. 1c) or octahedral In site ( $-483.65$  eV) (Fig. 1d), indicating that Ni atom prefers to substitute tetrahedral Zn site rather than tetrahedral/octahedral In sites. To further confirm such selective incorporation, two Ni atoms are simultaneously doped into the lattices of  $ZnIn_2S_4$ . As displayed in Figs. 1e and S1, the substitution of two Ni atoms for the tetrahedral Zn sites assures the lowest total energy ( $-487.63$  eV), again consolidating the preference of incorporated Ni atoms occupancy of tetrahedral Zn sites. Besides, the formation energy of Fermi level ( $E_f$ ) with different types and number of atoms replaced by Ni atoms was calculated. As summarized in Table S1, whether one or two Ni atoms incorporation, the substitution of tetrahedral Zn sites by Ni atoms leads to a lower  $E_f$ , uncovering that Ni atoms prefer to replace Zn sites rather than In sites in  $ZnIn_2S_4$ . Therefore,  $ZnIn_2S_4$  with Ni substitution for tetrahedral Zn is chosen for the following DFT simulations. The calculated density of state (DOS) manifests that the valence band maximum (VBM) of  $ZnIn_2S_4$  is mainly comprised of the S 3p orbital (Figs. 1f and S2). Upon the substitution of Ni atom for tetrahedral Zn site, the calculated DOS of Ni-ZnIn<sub>2</sub>S<sub>4</sub> shows an improved DOS at VBM as compared to that of bare  $ZnIn_2S_4$  (Fig. 1f), which suggests that Ni doping can induce more charge-carriers to participate into catalytic reaction. Besides, a shortened band gap and an

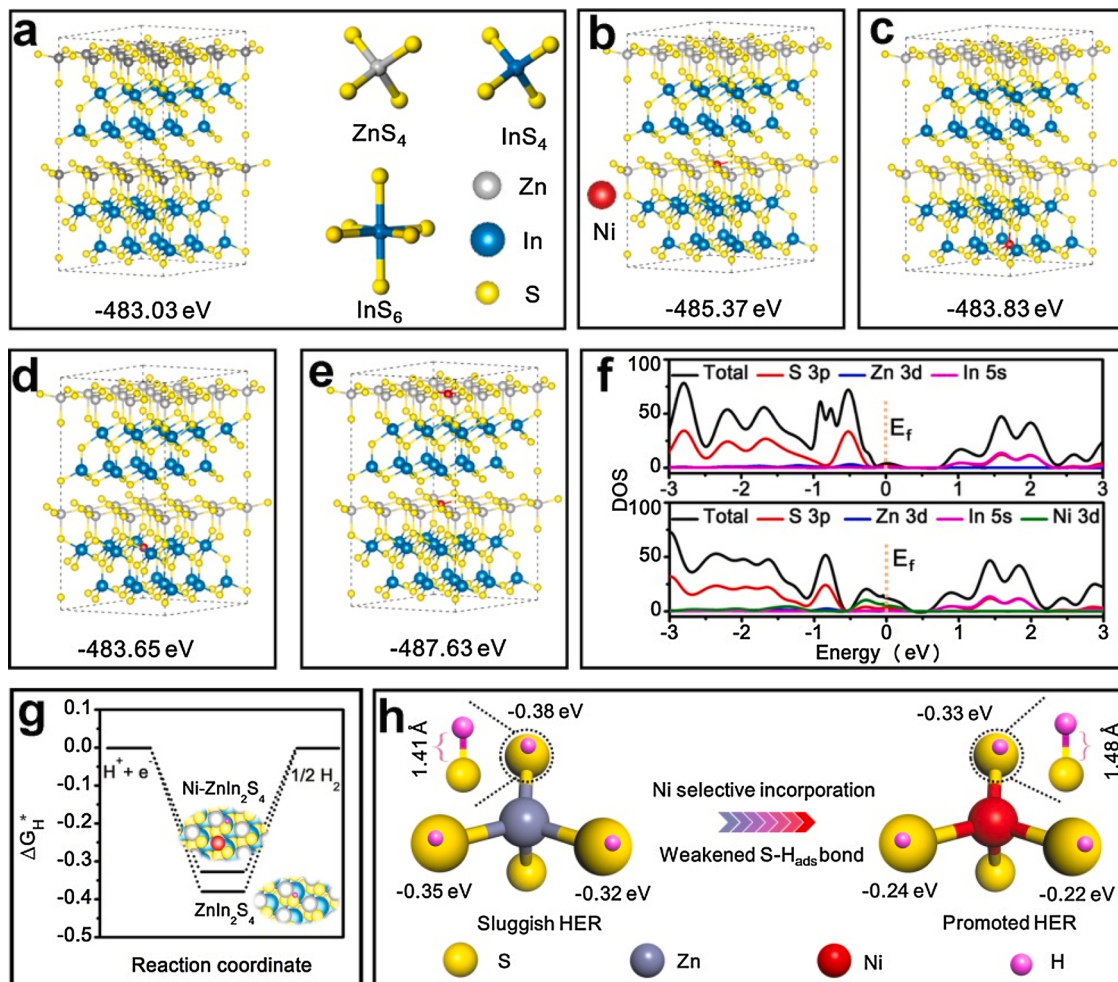


**Fig. 1.** Theoretical investigation of preference Ni dopant occupation sites in  $ZnIn_2S_4$  atomic layers. (a) Pristine  $ZnIn_2S_4$  crystal structure. (b) One Ni atom doping into tetrahedral Zn site. (c) One Ni atom doping into tetrahedral In site. (d) One Ni atom doping into octahedral In site. (e) Two Ni atoms doping into tetrahedral Zn sites. (f) Calculated DOS and (g) hydrogen adsorption free energy of  $ZnIn_2S_4$  and  $Ni-ZnIn_2S_4$ . (h) The comparison of adsorption free energy of H of different neighboring S atoms adsorption site and S-H<sub>ads</sub> bond length before and after Ni doping.

elevated DOS at Fermi level after Ni incorporation can be observed in Figs. 1f and S2, unraveling an extended light absorption range and improved electric conductivity, respectively, thus which are expected to have a high charge separation efficiency for Ni-ZnIn<sub>2</sub>S<sub>4</sub>. Furthermore, the newly generated band induced by Ni incorporation near Fermi level contributes to maneuver the H adsorption and desorption properties on S sites according to the Kohn-Sham orbitals theory [43].

Additionally, we scrutinize the electronic structure of S sites to elucidate the effects of Ni doping on the S—H<sub>ads</sub> bond. As indicated in Fig. 1g, the Gibbs free energy of the intermediate state ( $\Delta G_{H^*}$ ), a vital indicator correlated with the HER performance, was calculated. The calculation results demonstrate that Ni-ZnIn<sub>2</sub>S<sub>4</sub> offers a relatively moderate  $\Delta G_{H^*}$  of  $-0.33$  eV as compared to bare ZnIn<sub>2</sub>S<sub>4</sub>, revealing the optimized H adsorption and desorption capabilities for hydrogen evolution on Ni-ZnIn<sub>2</sub>S<sub>4</sub>. To further corroborate such positive effects of Ni doping on weakening the S—H<sub>ads</sub> bond energy, we investigate the adsorption free energy change of the neighboring S atoms and the SH—<sub>ads</sub> bond length before and after Ni doping. As displayed in Figs. 1h and S3, the Ni incorporation into tetrahedral Zn site induce a weakened H adsorption behavior on neighboring S sites and increased S—H<sub>ads</sub> bond length, which help to promoting hydrogen desorption from S sites. Based on the forementioned theoretical results, we believe that the strategy of Ni doping into ZnIn<sub>2</sub>S<sub>4</sub> atomic layers can provide a feasible route to optimize the charge separation and hydrogen desorption property on ZnIn<sub>2</sub>S<sub>4</sub>.

### 3.2. Preparation and characterizations of catalyst

Inspired by theoretical calculations, we designed few-layer Ni doped ZnIn<sub>2</sub>S<sub>4</sub> (Ni-ZnIn<sub>2</sub>S<sub>4</sub>) nanosheets via an one-step solvothermal method, in which Zn(CH<sub>3</sub>COO)<sub>2</sub>, InCl<sub>3</sub>, and Ni(CH<sub>3</sub>COO)<sub>2</sub> with a mole ratio of 4:8:0.3, and thioacetamide served as metal and sulfur precursors, respectively. The atomic force microscope (AFM) measurements (Fig. 2a–b) obviously demonstrate that the average thickness of Ni-ZnIn<sub>2</sub>S<sub>4</sub> is around 5–6 nm, which is equivalent to the thickness of four/five-unit-cell ZnIn<sub>2</sub>S<sub>4</sub> slab (Fig. 2a, inset). Such ultrathin structure endows Ni-ZnIn<sub>2</sub>S<sub>4</sub> with high surface area of  $94.8\text{ m}^2\text{ g}^{-1}$  (Fig. S4), which is slightly larger than the bare ZnIn<sub>2</sub>S<sub>4</sub>, indicating more active sites on the surface of Ni-ZnIn<sub>2</sub>S<sub>4</sub>. X-ray diffraction (XRD) patterns (Fig. 2c) confirmed the successful synthesis of the hexagonal phase of ZnIn<sub>2</sub>S<sub>4</sub>. It is noted that the typical peak of Ni-ZnIn<sub>2</sub>S<sub>4</sub> shifts towards higher diffraction angles relative to that of ZnIn<sub>2</sub>S<sub>4</sub> (Fig. 2c, inset), indicating Ni incorporation into the lattices of ZnIn<sub>2</sub>S<sub>4</sub>. The Ni doping concentration (1.0 wt. %) is determined by inductively coupled plasma mass spectrometry (ICP-MS) (Table S2). The transmission electron microscopy (TEM) image (Fig. 2d) reveals that the Ni-ZnIn<sub>2</sub>S<sub>4</sub> sample has a hexagonal ultrathin structure with lateral size of 50–150 nm. Of note, the incorporation of Ni atoms has a negligible effect on the morphology (Fig. S5a) and thickness (Fig. S5b) of ZnIn<sub>2</sub>S<sub>4</sub> nanosheets. The high resolution transmission electron microscopy (HRTEM) image (Fig. 2e) of Ni-ZnIn<sub>2</sub>S<sub>4</sub> displays two sets of lattice fringes spacings of 0.33 nm, corresponding to the (101) plane of ZnIn<sub>2</sub>S<sub>4</sub> [44,45], and the interaxial angle of 120° is well consistent with the hexagonal phase of ZnIn<sub>2</sub>S<sub>4</sub> [46–48]. Of note, the lattice fringe of the (101) plane of Ni-ZnIn<sub>2</sub>S<sub>4</sub> is

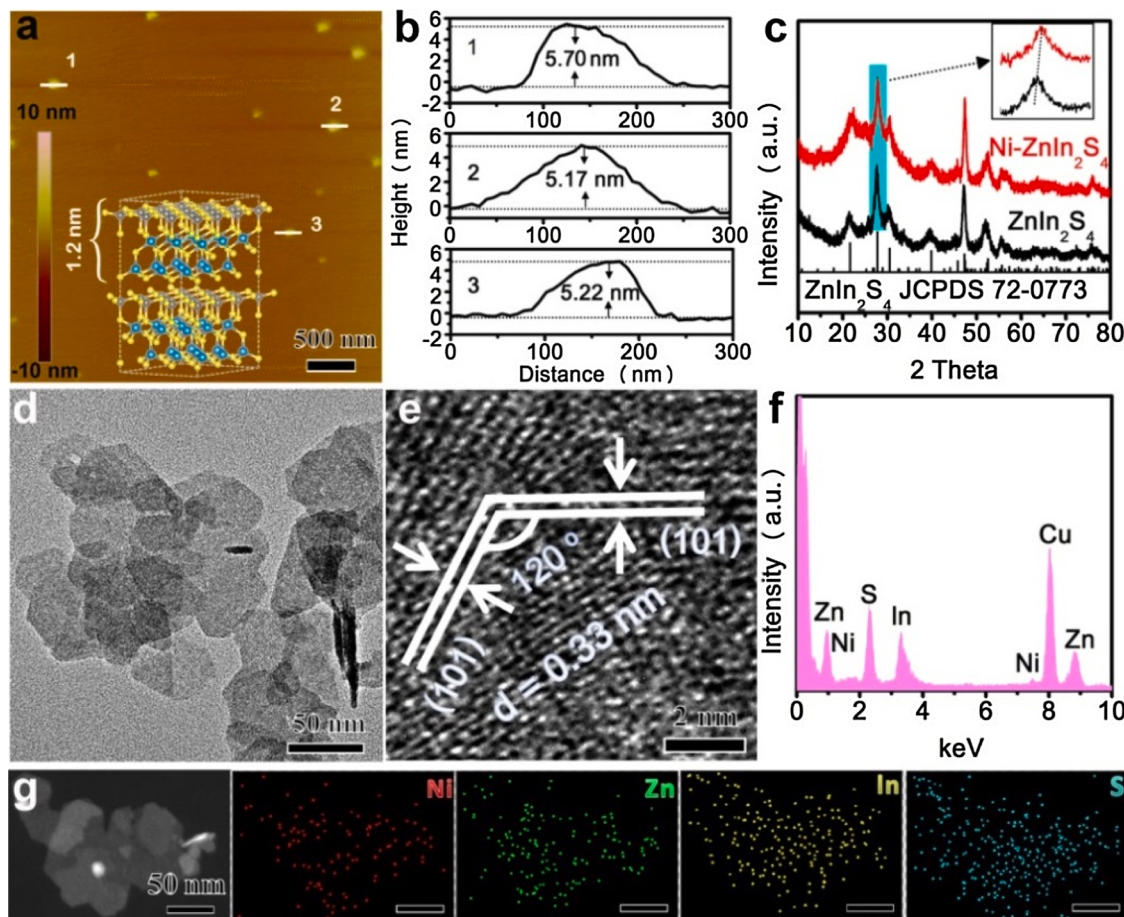


**Fig. 2.** (a) AFM image (the inset is the structural model of the standard unit cell) and (b) the corresponding height profile of Ni-ZnIn<sub>2</sub>S<sub>4</sub>. (c) XRD patterns of ZnIn<sub>2</sub>S<sub>4</sub> and Ni-ZnIn<sub>2</sub>S<sub>4</sub>, and the inset is the enlarged part of the cyan area. (d) TEM and (e) HRTEM image of Ni-ZnIn<sub>2</sub>S<sub>4</sub>. (f) EDX spectrum and (g) the corresponding element mapping of Ni-ZnIn<sub>2</sub>S<sub>4</sub>. The forementioned Ni-ZnIn<sub>2</sub>S<sub>4</sub> sample refers to ZnIn<sub>2</sub>S<sub>4</sub> with 1 wt. % Ni doping concentration.

slightly less than that of pristine  $\text{ZnIn}_2\text{S}_4$  (Fig. S5c) owing to the lattice contraction by Ni incorporation, a fact which is associated with the smaller radius of  $\text{Ni}^{2+}$  relative to  $\text{Zn}^{2+}$ . The energy-dispersive X-ray (EDX) spectrum (Fig. 2f) and the corresponding element mapping (Fig. 2g) demonstrate that Ni, Zn, In, and S elements are uniformly dispersed on  $\text{Ni-ZnIn}_2\text{S}_4$ , indicating the successful incorporation of Ni atoms into the lattices of  $\text{ZnIn}_2\text{S}_4$ .

To elucidate the chemical status of  $\text{Ni-ZnIn}_2\text{S}_4$ , X-ray photoelectron spectroscopy (XPS) was performed. The core level of Ni 2p spectrum is deconvoluted into two spin-orbit peaks and two shakeup satellites (Fig. 3a). The one peak at 854.3 eV and the other peak at 873.6 eV are assigned to  $\text{Ni}^{2+}$  2p<sub>3/2</sub> and  $\text{Ni}^{2+}$  2p<sub>1/2</sub>, respectively, suggesting the formation of Ni-S bond in  $\text{ZnIn}_2\text{S}_4$  [49,50]. The Zn 2p XPS spectra (Fig. 3b) demonstrate that the binding energies of Zn 2p<sub>1/2</sub> (1045.00 eV) and Zn 2p<sub>3/2</sub> (1022.90 eV) in  $\text{Ni-ZnIn}_2\text{S}_4$  are higher than those of Zn 2p<sub>1/2</sub> (1044.80 eV) and Zn 2p<sub>3/2</sub> (1021.70 eV) in  $\text{ZnIn}_2\text{S}_4$ , whereas the binding energies of In 3d in  $\text{Ni-ZnIn}_2\text{S}_4$  almost keep the same as those in  $\text{ZnIn}_2\text{S}_4$  (Fig. 3c), manifesting Ni selectively doping into tetrahedral Zn sites rather than In sites, which is in a good agreement with the theoretical calculations results. The S 2p XPS spectrum for  $\text{Ni-ZnIn}_2\text{S}_4$  is deconvoluted into S 2p<sub>1/2</sub> and 2p<sub>3/2</sub>. Compared with bare  $\text{ZnIn}_2\text{S}_4$ , the S 2p typical peaks of  $\text{Ni-ZnIn}_2\text{S}_4$  shift to higher binding energy, a fact which is well associated with the lower electron-donating ability of Ni versus Zn. Such change of S 2p binding energy in  $\text{Ni-ZnIn}_2\text{S}_4$  also uncovers the formation of neighboring S atoms with a decreased electron density, which contributes to weakening the S-H<sub>ads</sub> bond. The decreased electron density on S sites was further revealed by the calculated charge difference. As shown in Fig. 3e, once one tetrahedral Zn site is replaced by one Ni atom, the accumulated electron density on the Ni atoms can be observed as a result of larger electronegativity of Ni than Zn. Accordingly, the electron density on S atoms decreases owing to the reduced electron from Ni to S. Furthermore, compared with one Ni atom doping, two Ni atoms incorporation leads to electronic delocalization from the outer orbitals of Ni atom, which indicates that more charge carriers can

participate in the catalytic reaction directly, thus benefiting the improvement of HER performance.

### 3.3. Investigations of charge transfer pathway and efficiency

Apart from electronic structure modulation of catalytic sites, Ni incorporation strongly influences the band structure of  $\text{ZnIn}_2\text{S}_4$ , as validated by ultraviolet-visible spectrum. As demonstrated in Fig. S6, the band gap of  $\text{Ni-ZnIn}_2\text{S}_4$  is calculated to be 1.76 eV, which is smaller than that of bare  $\text{ZnIn}_2\text{S}_4$  (1.89 eV), indicating an extended visible light absorption for  $\text{Ni-ZnIn}_2\text{S}_4$ . The VB positions of  $\text{ZnIn}_2\text{S}_4$  and  $\text{Ni-ZnIn}_2\text{S}_4$  were determined by VB-XPS. As shown in Fig. S7a, the VB position of  $\text{Ni-ZnIn}_2\text{S}_4$  increases to 0.21 eV relative to that of bare  $\text{ZnIn}_2\text{S}_4$ . Accordingly, the conduction band (CB) of  $\text{Ni-ZnIn}_2\text{S}_4$  is estimated to be upshifted by 0.08 eV (Fig. S7b), corresponding to the enhanced reduction potential of photo-induced electrons on CB. In addition to the extended light absorption range, the suppressed recombination of photo-excited charge carriers is extraordinarily crucial for photocatalytic HER performance. To unveil the underlying influences of Ni selective doping on the charge separation efficiency, steady-state photoluminescence (PL) spectra were employed. The emission peak located at 545 nm is indexed to the band-to-band transition [45]. As shown in Fig. 4a,  $\text{Ni-ZnIn}_2\text{S}_4$  exhibits a much decreased PL intensity in regard to pristine  $\text{ZnIn}_2\text{S}_4$ , revealing a suppressed band-to-band transition and a highly efficient separation of photo-generated electrons-hole pairs in  $\text{Ni-ZnIn}_2\text{S}_4$ . Correspondingly, the time-resolved PL decay spectra (Fig. 4b) demonstrates that Ni doping endows  $\text{ZnIn}_2\text{S}_4$  with increased average PL lifetimes (Table S3), implying that more photo-induced charge carriers can be involved in the photocatalytic reaction. Such improved charge separation efficiency was further evidenced by the transient photoelectric response and the electrochemical impedance spectra (EIS). As indicated in Fig. 4c, it is obvious that the photocurrent density of  $\text{Ni-ZnIn}_2\text{S}_4$  is higher than that of  $\text{ZnIn}_2\text{S}_4$ . On the other hand,  $\text{Ni-ZnIn}_2\text{S}_4$  also enables a reduced interfacial charge transfer resistance

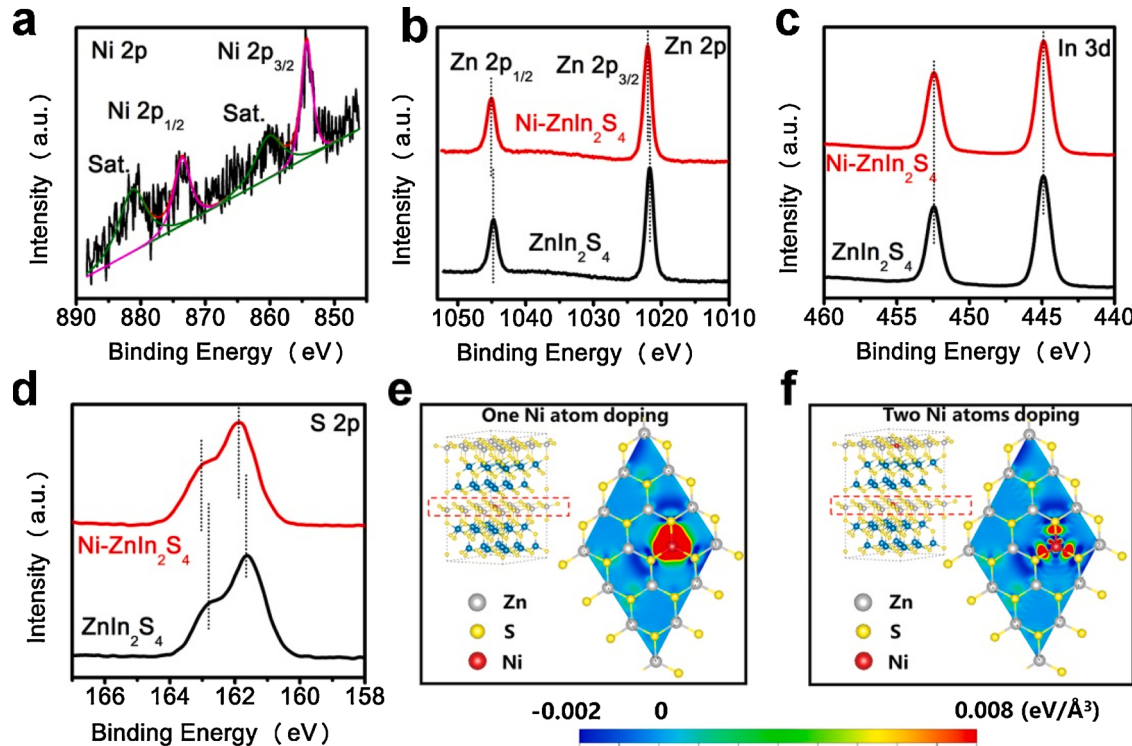


**Fig. 3.** (a) High-resolution Ni 2p XPS spectrum of  $\text{Ni-ZnIn}_2\text{S}_4$ . (b) High-resolution XPS spectra of Zn 2p, (c) In 3d, (d) S2p of  $\text{ZnIn}_2\text{S}_4$  and  $\text{Ni-ZnIn}_2\text{S}_4$ . The fore-mentioned  $\text{Ni-ZnIn}_2\text{S}_4$  sample refers to  $\text{ZnIn}_2\text{S}_4$  with 1 wt.% Ni doping concentration. Differential charge density distributions with one Ni atom substitution for Zn (e) and with two Ni atoms substitution for Zn (f), plotted from -0.002 (blue) to 0.008 eV (red).

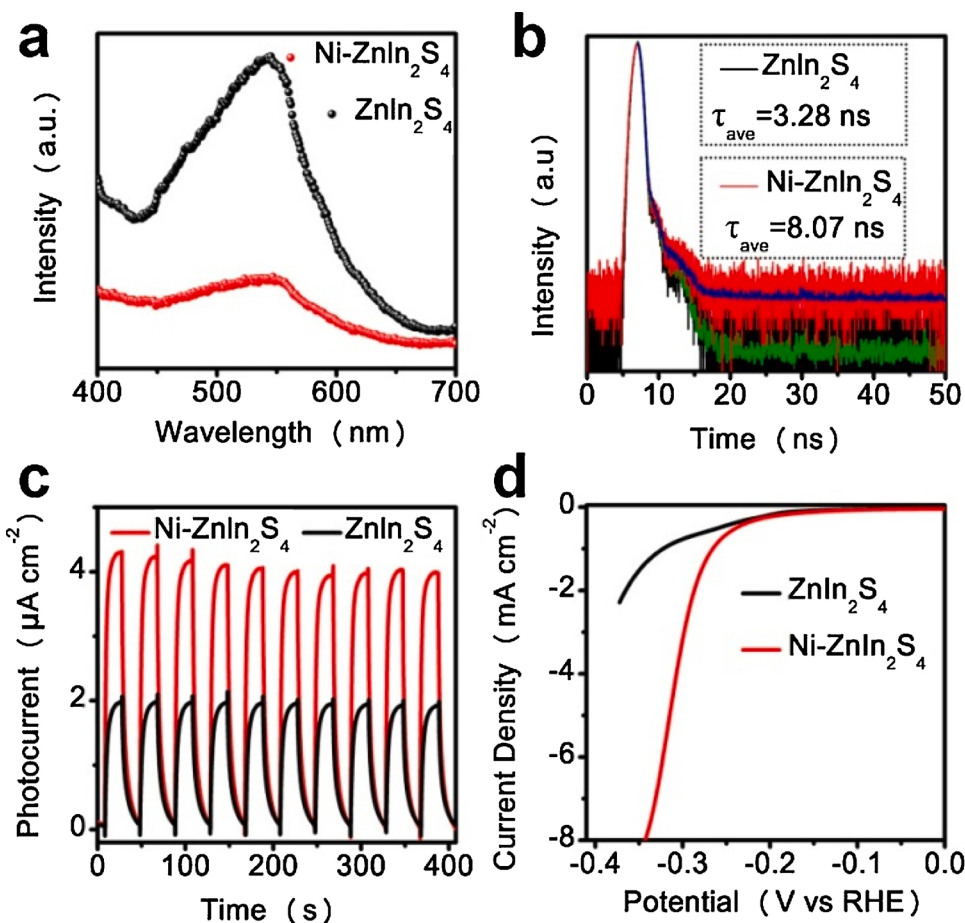


**Fig. 4.** (a) PL spectra, (b) time-resolved PL decay spectra, (c) transient photocurrents, (d) polarization curves of  $\text{ZnIn}_2\text{S}_4$  and  $\text{Ni-ZnIn}_2\text{S}_4$  with 1 wt.% Ni doping concentration.

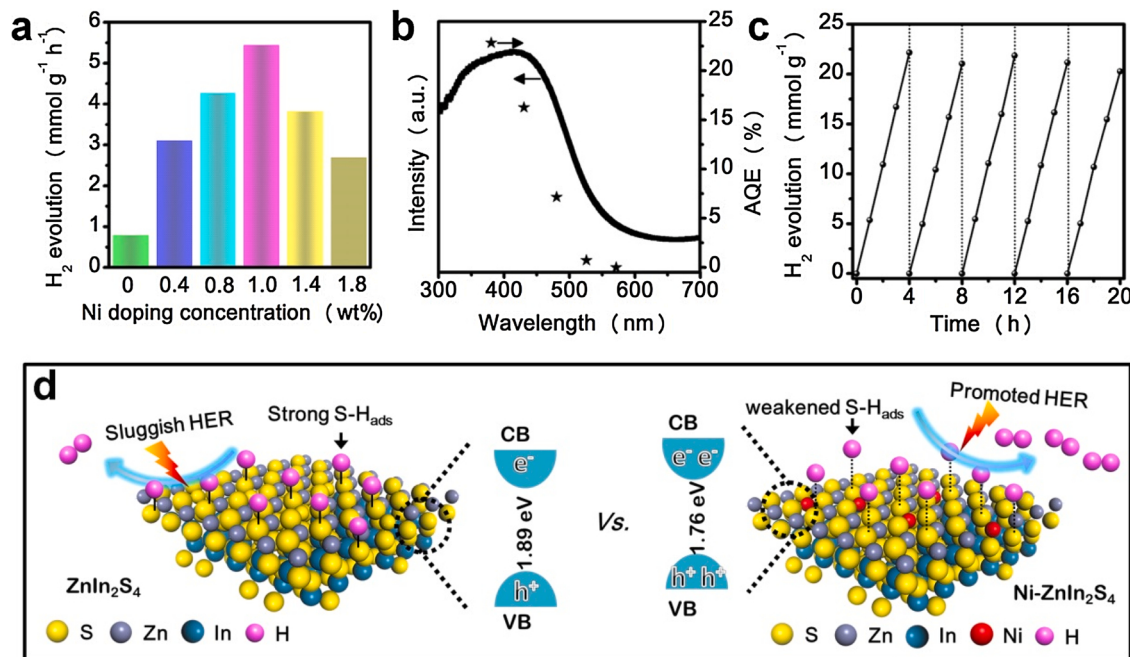


**Fig. 5.** (a) Photocatalytic hydrogen evolution rate of  $\text{ZnIn}_2\text{S}_4$  with different Ni doping concentrations. (b) Wavelength dependence of AQE of  $\text{Ni-ZnIn}_2\text{S}_4$  with 1 wt. % Ni doping concentration. (c) Recycling  $\text{H}_2$  evolution tests for  $\text{Ni-ZnIn}_2\text{S}_4$  with 1 wt. % Ni doping concentration. (d) Schematic illustration of light absorption, charge separation, and hydrogen evolution process on  $\text{ZnIn}_2\text{S}_4$  and  $\text{Ni-ZnIn}_2\text{S}_4$ .

as compared to bare  $\text{ZnIn}_2\text{S}_4$  by comparing the Nyquist semicircle diameter in the EIS (Fig. S8). Besides, linear sweep voltammetry (LSV) measurements were utilized to evaluate the hydrogen evolution ability on  $\text{ZnIn}_2\text{S}_4$  and  $\text{Ni-ZnIn}_2\text{S}_4$ . It can be clearly observed that  $\text{Ni-ZnIn}_2\text{S}_4$  enables a higher cathodic current density for HER relative to  $\text{ZnIn}_2\text{S}_4$  (Fig. 4d), which is attributed to the optimized H adsorption and desorption energy on S sites induced by Ni incorporation.

### 3.4. Photocatalytic hydrogen evolution activity and mechanism

In the view of simultaneous realization both of improved charge separation efficiency and the weakened S—H<sub>ads</sub> bond, an enhanced photocatalytic hydrogen production performance can be expected. Here, we investigated the hydrogen evolution performance of pristine  $\text{ZnIn}_2\text{S}_4$  and  $\text{Ni-ZnIn}_2\text{S}_4$  in an aqueous solution containing 10 vol. % triethanolamine (TEOA) under simulated solar light irradiation. As shown in Fig. 5a, 1 wt. % Ni doping leads to a high hydrogen evolution rate of 5.43 mmol g<sup>-1</sup> h<sup>-1</sup>, approximately 7 times higher than bare  $\text{ZnIn}_2\text{S}_4$  (0.78 mmol g<sup>-1</sup> h<sup>-1</sup>), which is similar to the trend of photocurrent response. As for the difference in increased ratios between photocurrent response and HER activity, some factors, including the usage of bias voltage, the introduction of electron donor, and the test atmosphere, should be responsible for it. To investigate the optimum Ni doping concentration, we synthesized  $\text{Ni-ZnIn}_2\text{S}_4$  nanosheets with different Ni doping levels (Figs. S9 and S10, Table S2) and confirm the doping concentration of 1 wt. % with the optimal hydrogen evolution activity. More notably,  $\text{Ni-ZnIn}_2\text{S}_4$  nanosheets with different Ni doping concentrations all exhibit enhanced HER activities as compared to the pristine  $\text{ZnIn}_2\text{S}_4$  nanosheets, a fact which is inextricably linked to the transmutation of electronic structure of active sites caused by Ni incorporation. Encouragingly, a considerably high apparent quantum efficiency (AQE) value of 16.26 % can be obtained at 420 nm, which outperforms most of previously reported  $\text{ZnIn}_2\text{S}_4$ -based HER photocatalysts (Table S4). It is noted that once the wavelength range extends beyond 500 nm, the AQE value for  $\text{Ni-ZnIn}_2\text{S}_4$  was distinctly reduced due to its poor light response ability in the corresponding visible-light region. The stability of  $\text{Ni-ZnIn}_2\text{S}_4$  with the optimal Ni doping level is further evaluated. As displayed in Fig. 5c,  $\text{Ni-ZnIn}_2\text{S}_4$  shows no noticeable decrement in photocatalytic H<sub>2</sub> evolution rate after 5 cycles. TEM observations (Fig. S11a), AFM image (Fig. S11b), and XRD patterns (Fig. S12) after the photocatalytic reaction demonstrate that the recovered  $\text{Ni-ZnIn}_2\text{S}_4$  sample maintains the same morphology and crystal structure as compared to the initial  $\text{Ni-ZnIn}_2\text{S}_4$  nanosheets, which further suggests the high stability of the  $\text{Ni-ZnIn}_2\text{S}_4$  photocatalyst for HER. Based on the above mentioned theoretical calculations and experimental studies, the schematic mechanism of photocatalytic HER in  $\text{Ni-ZnIn}_2\text{S}_4$  is illustrated in Fig. 5d. An extended light absorption range, improved electron reduction potential, and more charge carriers are first realized by Ni incorporation into Zn sites, which are essential prerequisites for improvement of HER performance. Subsequently, Ni doping reduces the electron density of S sites and weakens the S-H<sub>ads</sub> bond, which facilitates hydrogen desorption from S sites, thus achieving high-performance HER.

## 4. Conclusion

In conclusion, we fabricated Ni doped few-layer  $\text{ZnIn}_2\text{S}_4$  nanosheets as highly effective photocatalysts for HER. Ni incorporating into the lattices of  $\text{ZnIn}_2\text{S}_4$  leads to a narrow band gap, improved electron reduction potential, and more charge carrier through selective substitution for tetrahedral Zn sites, as uncovered by DFT calculations and XPS characterizations. More importantly, an optimal hydrogen adsorption free energy on  $\text{Ni-ZnIn}_2\text{S}_4$  is realized via subtly maneuvering the S-H<sub>ads</sub> bond energy. As a result, in comparison to pristine  $\text{ZnIn}_2\text{S}_4$ ,  $\text{Ni-ZnIn}_2\text{S}_4$  with optimized Ni doping level achieves an outstanding photocatalytic activity with a HER rate of 5.43 mmol g<sup>-1</sup> h<sup>-1</sup> and a high AQE value of

16.26 % at 420 nm. This work not only discloses the correlation between dopant and HER activity, but also highlights a feasible way for construction of high-performance HER photocatalysts.

## CRediT authorship contribution statement

The manuscript was written with contributions from Bocheng Qiu, Pan Huang, Cheng Lian, Yingxin Ma, Mingyang Xing, Honglai Liu, and Jinlong Zhang. All authors have approved the final version of the manuscript.

## Author contributions

J.Z. and B.Q. supervised the project and conceived the idea, designed all experiments, and wrote the manuscript. B.Q. and X.M. performed synthesis and characterizations of catalysts. B.Q. and X.M. carried out photo/electrocatalytic measurement and discussed the results. P.H. and C.L. performed the DFT simulations. M.X. and H.L. revised the manuscript and provided helpful suggestions. All authors provided constructive comments on the manuscript.

## Declaration of Competing Interest

The authors declare that they have no known competing financial interests or personal relationships that could have appeared to influence the work reported in this paper.

## Acknowledgments

This work was supported by National Natural Science Foundation of China (21972040, 21822603, 21773062, 91834301, 2207808), Shanghai Municipal Science and Technology (2018SHZDZX03, 20DZ2250400), Innovation Program of Shanghai Municipal Education Commission (2021-01-07-00-02-E00106), the Program of Introducing Talents of Discipline to Universities (B16017, B20031), and the Fundamental Research Funds for the Central Universities. Prof. B. C. Qiu gratefully acknowledges the support from Nanjing Agriculture University.

## Appendix A. Supplementary data

Supplementary material related to this article can be found, in the online version, at doi:<https://doi.org/10.1016/j.apcatb.2021.120518>.

## References

- [1] T. Takata, J. Jiang, Y. Sakata, M. Nakabayashi, N. Shibata, V. Nandal, K. Seki, T. Hisatomi, K. Domen, Photocatalytic water splitting with a quantum efficiency of almost unity, *Nature* 581 (2020) 411–414.
- [2] Z. Wang, C. Li, K. Domen, Recent developments in heterogeneous photocatalysts for solar-driven overall water splitting, *Chem. Soc. Rev.* 48 (2019) 2109–2125.
- [3] C.F. Fu, X. Wu, J. Yang, Material design for photocatalytic water splitting from a theoretical perspective, *Adv. Mater.* 30 (2018), 1802106.
- [4] B. Qiu, M. Xing, J. Zhang, Recent advances in three-dimensional graphene based materials for catalysis applications, *Chem. Soc. Rev.* 47 (2018) 2165–2216.
- [5] D. Zhao, Y. Wang, C.-L. Dong, Y.-C. Huang, J. Chen, F. Xue, S. Shen, L. Guo, Boron-doped nitrogen-deficient carbon nitride-based Z-scheme heterostructures for photocatalytic overall water splitting, *Nat. Energy* 6 (2021) 388–397.
- [6] B. Qiu, L. Cai, N. Zhang, X. Tao, Y. Chai, A ternary dumbbell structure with spatially separated catalytic sites for photocatalytic overall water splitting, *Adv. Sci.* 7 (2020), 1903568.
- [7] Q. Zhu, Z. Xu, Q. Yi, M. Nasir, M. Xing, B. Qiu, J. Zhang, Prolonged electron lifetime in sulfur vacancy-rich  $\text{ZnCdS}$  nanocages by interstitial phosphorus doping for photocatalytic water reduction, *Mater. Chem. Front.* 4 (2020) 3234–3239.
- [8] D. Zeng, L. Xiao, W.J. Ong, P. Wu, H. Zheng, Y. Chen, D.L. Peng, Hierarchical  $\text{ZnIn}_2\text{S}_4/\text{MoSe}_2$  nanoarchitectures for efficient noble-metal-free photocatalytic hydrogen evolution under visible light, *ChemSusChem* 10 (2017) 4624–4631.
- [9] L. Wang, Y. Zhang, L. Chen, H. Xu, Y. Xiong, 2D polymers as emerging materials for photocatalytic overall water splitting, *Adv. Mater.* 30 (2018), 1801955.
- [10] J. Liu, J. Ke, Y. Li, B. Liu, L. Wang, H. Xiao, S. Wang,  $\text{Co}_3\text{O}_4$  quantum dots/TiO<sub>2</sub> nanobelt hybrids for highly efficient photocatalytic overall water splitting, *Appl. Catal. B: Environ.* 236 (2018) 396–403.

- [11] B. Qiu, C. Wang, J. Wang, Z. Lin, N. Zhang, L. Cai, X. Tao, Y. Chai, Metal-free tellurene cocatalyst with tunable bandgap for enhanced photocatalytic hydrogen production, *Mater. Today Energy* 21 (2021), 100720.
- [12] X. Cai, Z. Zeng, Y. Liu, Z. Li, X. Gu, Y. Zhao, L. Mao, J. Zhang, Visible-light-driven water splitting by yolk-shell ZnIn<sub>2</sub>S<sub>4</sub>-based heterostructure without noble-metal co-catalyst and sacrificial agent, *Appl. Catal. B: Environ.* 297 (2021), 120391.
- [13] J. Wang, S. Lin, N. Tian, T. Ma, Y. Zhang, H. Huang, Nanostructured metal sulfides: classification, modification strategy, and solar-driven CO<sub>2</sub> reduction application, *Adv. Funct. Mater.* 31 (2021), 2008008.
- [14] S. Zhang, X. Liu, C. Liu, S. Luo, L. Wang, T. Cai, Y. Zeng, J. Yuan, W. Dong, Y. Pei, MoS<sub>2</sub> quantum dot growth induced by S vacancies in a ZnIn<sub>2</sub>S<sub>4</sub> monolayer: atomic-level heterostructure for photocatalytic hydrogen production, *ACS Nano* 12 (2018) 751–758.
- [15] J. Lee, H. Kim, T. Lee, W. Jang, K.H. Lee, A. Soon, Revisiting polytypism in hexagonal ternary sulfide ZnIn<sub>2</sub>S<sub>4</sub> for photocatalytic hydrogen production within the Z-scheme, *Chem. Mater.* 31 (2019) 9148–9155.
- [16] S. Wang, Y. Wang, S.L. Zhang, S.Q. Zang, X.W. Lou, Supporting ultrathin ZnIn<sub>2</sub>S<sub>4</sub> nanosheets on Co/N-doped graphitic carbon nanocages for efficient photocatalytic H<sub>2</sub> generation, *Adv. Mater.* 31 (2019), 1903404.
- [17] S. Zhang, M. Du, Z. Xing, Z. Li, K. Pan, W. Zhou, Defect-rich and electron-rich mesoporous Ti-MOFs based NH<sub>2</sub>-MIL-125 (Ti)@ZnIn<sub>2</sub>S<sub>4</sub>/Cds hierarchical tandem heterojunctions with improved charge separation and enhanced solar-driven photocatalytic performance, *Appl. Catal. B: Environ.* 262 (2020), 118202.
- [18] X. Jiao, X. Li, X. Jin, Y. Sun, J. Xu, L. Liang, H. Ju, J. Zhu, Y. Pan, W. Yan, Partially oxidized SnS<sub>2</sub> atomic layers achieving efficient visible-light-driven CO<sub>2</sub> reduction, *J. Am. Chem. Soc.* 139 (2017) 18044–18051.
- [19] L. Meng, D. Rao, W. Tian, F. Cao, X. Yan, L. Li, Simultaneous manipulation of O-doping and metal vacancy in atomically thin Zn<sub>10</sub>In<sub>16</sub>S<sub>34</sub> nanosheet arrays toward improved photoelectrochemical performance, *Angew. Chem. Int. Ed.* 57 (2018) 16882–16887.
- [20] L. Meng, S. Wang, F. Cao, W. Tian, R. Long, L. Li, Doping-induced amorphization, vacancy, and gradient energy band in SnS<sub>2</sub> nanosheet arrays for improved photoelectrochemical water splitting, *Angew. Chem. Int. Ed.* 58 (2019) 6761–6765.
- [21] W. Yang, L. Zhang, J. Xie, X. Zhang, Q. Liu, T. Yao, S. Wei, Q. Zhang, Y. Xie, Enhanced photoexcited carrier separation in oxygen-doped ZnIn<sub>2</sub>S<sub>4</sub> nanosheets for hydrogen evolution, *Angew. Chem. Int. Ed.* 55 (2016) 6716–6720.
- [22] Z. Guan, Z. Xu, Q. Li, P. Wang, G. Li, J. Yang, AgIn<sub>5</sub>S<sub>8</sub> nanoparticles anchored on 2D layered ZnIn<sub>2</sub>S<sub>4</sub> to form OD/2D heterojunction for enhanced visible-light photocatalytic hydrogen evolution, *Appl. Catal. B: Environ.* 227 (2018) 512–518.
- [23] X. Shi, L. Mao, P. Yang, H. Zheng, M. Fujitsuka, J. Zhang, T. Majima, Ultrathin ZnIn<sub>2</sub>S<sub>4</sub> nanosheets with active (110) facet exposure and efficient charge separation for cocatalyst free photocatalytic hydrogen evolution, *Appl. Catal. B: Environ.* 265 (2020), 118616.
- [24] J. Pan, G. Zhang, Z. Guan, Q. Zhao, G. Li, J. Yang, Q. Li, Z. Zou, Anchoring Ni single atoms on sulfur-vacancy-enriched ZnIn<sub>2</sub>S<sub>4</sub> nanosheets for boosting photocatalytic hydrogen evolution, *J. Energy Chem.* 58 (2021) 408–414.
- [25] G. Yang, H. Ding, D. Chen, J. Feng, Q. Hao, Y. Zhu, Construction of urchin-like ZnIn<sub>2</sub>S<sub>4</sub>-Au-TiO<sub>2</sub> heterostructure with enhanced activity for photocatalytic hydrogen evolution, *Appl. Catal. B: Environ.* 234 (2018) 260–267.
- [26] Y. Wu, X. Liu, D. Han, X. Song, L. Shi, Y. Song, S. Niu, Y. Xie, J. Cai, S. Wu, Electron density modulation of NiCo<sub>2</sub>S<sub>4</sub> nanowires by nitrogen incorporation for highly efficient hydrogen evolution catalysis, *Nat. Commun.* 9 (2018) 1425–1433.
- [27] G. Zuo, Y. Wang, W.L. Teo, A. Xie, Y. Guo, Y. Dai, W. Zhou, D. Jana, Q. Xian, W. Dong, Ultrathin ZnIn<sub>2</sub>S<sub>4</sub> nanosheets anchored on Ti<sub>3</sub>C<sub>2</sub>TX MXene for photocatalytic H<sub>2</sub> evolution, *Angew. Chem. Int. Ed.* 59 (2020) 11287–11292.
- [28] B. Qiu, L. Cai, Y. Wang, X. Guo, S. Ma, Y. Zhu, Y.H. Tsang, Z. Zheng, R. Zheng, Y. Chai, Phosphorus incorporation into Co<sub>3</sub>S<sub>8</sub> nanocages for highly efficient oxygen evolution catalysis, *Small* 15 (2019), 1904507.
- [29] G. Gong, Y. Liu, B. Mao, L. Tan, Y. Yang, W. Shi, Ag doping of Zn-In-S quantum dots for photocatalytic hydrogen evolution: simultaneous bandgap narrowing and carrier lifetime elongation, *Appl. Catal. B: Environ.* 216 (2017) 11–19.
- [30] H. She, Y. Sun, S. Li, J. Huang, L. Wang, G. Zhu, Q. Wang, Synthesis of non-noble metal nickel doped sulfide solid solution for improved photocatalytic performance, *Appl. Catal. B: Environ.* 245 (2019) 439–447.
- [31] F. Lei, L. Zhang, Y. Sun, L. Liang, K. Liu, J. Xu, Q. Zhang, B. Pan, Y. Luo, Y. Xie, Atomic-layer-confined doping for atomic-level insights into visible-light water splitting, *Angew. Chem.* 127 (2015) 9398–9402.
- [32] C. Wang, Z. Chen, H. Jin, C. Cao, J. Li, Z. Mi, Enhancing visible-light photoelectrochemical water splitting through transition-metal doped TiO<sub>2</sub> nanorod arrays, *J. Mater. Chem. A* 2 (2014) 17820–17827.
- [33] X. Jiao, K. Zheng, L. Liang, X. Li, Y. Sun, Y. Xie, Fundamentals and challenges of ultrathin 2D photocatalysts in boosting CO<sub>2</sub> photoreduction, *Chem. Soc. Rev.* 49 (2020) 6592–6604.
- [34] Y. Ma, B. Qiu, J. Zhang, M. Xing, Vacancy engineering of ultrathin 2D materials for photocatalytic CO<sub>2</sub> reduction, *ChemNanoMat* 7 (2021) 368–379.
- [35] S.-m. Chang, W.-s. Liu, Surface doping is more beneficial than bulk doping to the photocatalytic activity of vanadium-doped TiO<sub>2</sub>, *Appl. Catal. B: Environ.* 101 (2011) 333–342.
- [36] J. Di, C. Yan, A.D. Handoko, Z.W. Seh, H. Li, Z. Liu, Ultrathin two-dimensional materials for photo-and electrocatalytic hydrogen evolution, *Mater. Today* 21 (2018) 749–770.
- [37] J. Xiong, J. Di, J. Xia, W. Zhu, H. Li, Surface defect engineering in 2D nanomaterials for photocatalysis, *Adv. Funct. Mater.* 28 (2018), 1801983.
- [38] H. Wang, X. Zhang, Y. Xie, Photocatalysis in two-dimensional black phosphorus: the roles of many-body effects, *ACS Nano* 12 (2018) 9648–9653.
- [39] S. Wang, B.Y. Guan, X. Wang, X.W.D. Lou, Formation of hierarchical Co<sub>9</sub>S<sub>8</sub>@ZnIn<sub>2</sub>S<sub>4</sub> heterostructured cages as an efficient photocatalyst for hydrogen evolution, *J. Am. Chem. Soc.* 140 (2018) 15145–15148.
- [40] G. Kresse, J. Furthmüller, Efficient iterative schemes for ab initio total-energy calculations using a plane-wave basis set, *Phys. Rev. B* 54 (1996) 11169.
- [41] G. Kresse, J. Furthmüller, Efficiency of ab-initio total energy calculations for metals and semiconductors using a plane-wave basis set, *Comp. Mater. Sci.* 6 (1996) 15–50.
- [42] G. Kresse, J. Hafner, Ab initio molecular-dynamics simulation of the liquid-metal–amorphous–semiconductor transition in germanium, *Phys. Rev. B* 49 (1994) 14251.
- [43] J. Greeley, T.F. Jarillo, J. Bonde, I. Chorkendorff, J.K. Nørskov, Computational high-throughput screening of electrocatalytic materials for hydrogen evolution, *Nat. Mater.* 5 (2006) 909–913.
- [44] Y. Sun, C. Xue, L. Chen, Y. Li, S. Guo, Y. Shen, F. Dong, G. Shao, P. Zhang, Enhancement of interfacial charge transportation through construction of 2D-2D p-n heterojunctions in hierarchical 3D CNFs/MoS<sub>2</sub>/ZnIn<sub>2</sub>S<sub>4</sub> composites to enable high-efficiency photocatalytic hydrogen evolution, *Solar RRL* 5 (2021), 2000722.
- [45] P. Wang, Z. Shen, Y. Xia, H. Wang, L. Zheng, W. Xi, S. Zhan, Atomic insights for optimum and excess doping in photocatalysis: a case study of few-layer Cu-ZnIn<sub>2</sub>S<sub>4</sub>, *Adv. Funct. Mater.* 29 (2019), 1807013.
- [46] J. Wang, Y. Chen, W. Zhou, G. Tian, Y. Xiao, H. Fu, H. Fu, Cubic quantum dot/hexagonal microsphere ZnIn<sub>2</sub>S<sub>4</sub> heterophase junctions for exceptional visible-light-driven photocatalytic H<sub>2</sub> evolution, *J. Mater. Chem. A* 5 (2017) 8451–8460.
- [47] Y. He, H. Rao, K. Song, J. Li, Y. Yu, Y. Lou, C. Li, Y. Han, Z. Shi, S. Feng, 3D hierarchical ZnIn<sub>2</sub>S<sub>4</sub> nanosheets with rich Zn vacancies boosting photocatalytic CO<sub>2</sub> reduction, *Adv. Funct. Mater.* 29 (2019), 1905153.
- [48] Y. Qin, H. Li, J. Lu, Y. Feng, F. Meng, C. Ma, Y. Yan, M. Meng, Synergy between van der waals heterojunction and vacancy in ZnIn<sub>2</sub>S<sub>4</sub>/g-C<sub>3</sub>N<sub>4</sub> 2D/2D photocatalysts for enhanced photocatalytic hydrogen evolution, *Appl. Catal. B: Environ.* 277 (2020), 119254.
- [49] Q. Zhang, Y. Xiao, Y. Li, K. Zhao, H. Deng, Y. Lou, J. Chen, L. Cheng, NiS-decorated ZnO/ZnS nanorod heterostructures for enhanced photocatalytic hydrogen production: insight into the role of NiS, *Solar RRL* 4 (2020), 1900568.
- [50] L. An, J. Feng, Y. Zhang, R. Wang, H. Liu, G.C. Wang, F. Cheng, P. Xi, Epitaxial heterogeneous interfaces on N-NiMoO<sub>4</sub>/NiS<sub>2</sub> nanowires/nanosheets to boost hydrogen and oxygen production for overall water splitting, *Adv. Funct. Mater.* 29 (2019), 1805298.